Transient absorption measurements of excitonic dynamics in math xmlns="http://www.w3.org/1998/Math/MathML">mrow>mn>3/mn>mi>R/mi>/mrow>mtext>−/mtext>msub>mrow>mi>MoS/mi>/mrow>mn>2/mn>/msub>/math>

Gbenga Agunbiade, Neema Rafizadeh, Ryan J. Scott, and Hui Zhao

Transient absorption measurements of excitonic dynamics in 3R-MoS$_2$

Gbenga Agunbiade, Neema Rafizadeh, Ryan J. Scott, and Hui Zhao*

Department of Physics and Astronomy, The University of Kansas, Lawrence, Kansas 66045, United States

(Dated: December 13, 2023)

The excitonic dynamics in MoS$_2$ monolayer, bilayer, and bulk flakes with different stacking orders, namely 3R and 2H, are investigated through transient absorption spectroscopy at room temperature. Samples are obtained by the mechanical exfoliation of bulk MoS$_2$ crystals with 3R and 2H stacking orders. Photoluminescence spectroscopy is performed to characterize and compare the samples. Time-resolved differential reflection measurements reveal that monolayer flakes exfoliated from the 3R and 2H crystals exhibit similar exciton lifetimes of a few picoseconds. However, the exciton lifetime in the 3R bilayer flake is approximately 85 ps, about twice as long as that in the 2H bilayer. This prolonged exciton lifetime is attributed to the reduction of the electron-hole wavefunction overlap in the 3R bilayer due to the built-in polarization. Similarly, in bulk 3R MoS$_2$, the exciton lifetime is around 220 ps, approximately twice as long as those in bulk 2H MoS$_2$. The extension of the exciton lifetime in 3R transition metal dichalcogenides could be advantageous for their applications in optoelectronic devices.

I. INTRODUCTION

Semiconducting transition metal dichalcogenides (TMDs), such as MoS$_2$ and WS$_2$, have emerged as an important class of materials with a multitude of novel properties. These layered compounds possess remarkable electronic properties that are attractive for many applications. [1, 2] The band gap of TMDs can be precisely engineered by varying their thickness and strain, enabling fine-tuning of their electronic properties for specific applications. [3, 4] This tunability, combined with their high charge carrier mobility, makes them ideal channel materials for high-performance transistors, flexible electronics, and integrated circuits. [5, 6] Moreover, semiconducting TMDs exhibit strong light-matter interactions, leading to efficient absorption and emission of photons. This property can be harnessed in photodetectors, light-emitting diodes, and photovoltaic devices. [7–10]

The majority of semiconducting TMDs adopt the hexagonal 2H structure, extensively studied in the literature. However, there is a growing interest to explore a less common but thermodynamically stable stacking order, 3R, which exhibits a rhombohedral lattice structure. [11] Figure 1 highlights the differences between the two stacking orders. In the AA stacking (a), two monolayers (1Ls) are stacked without any rotation or sliding. This stacking order is less stable with a relatively large interlayer distance. A 2H MX$_2$ bilayer (2L) is obtained by rotating the top layer by π around a vertical axis and sliding it, aligning its M and X atoms with the X and M atoms in the bottom layer, as shown in (b). This arrangement restores mirror symmetry, eliminating several interesting physical processes associated with low-symmetry lattices, such as second-order nonlinear optical processes and valley-selective population. Alternatively, sliding the top layer of the AA 2L results in two nonequivalent configurations - an AB stacking with the M atoms in the top layer align with the X atoms in the bottom layer (c), and a BA stacking with the X atoms on top aligning with the M atoms at the bottom (d). In each 3R

stacking, a built-in polarization exists, as shown by the blue arrows in Fig. 1. If the two layers are identified by the type of atoms aligned with the other layer, the AB and BA 3R stacking can be referred to as MX and XM orders, respectively. The built-in polarization always points from the "X layer" to the "M layer".

Recently, 3R MX$_2$ 2Ls have been successfully produced directly by chemical vapor deposition (CVD) [12–16] and by mechanical exfoliation of bulk 3R crystals. [17] Since the inversion symmetry and the mirror symmetry are broken by the lack of rotation and the layer sliding, respectively, 3R MX$_2$ 2Ls show strong second-order nonlinear optical effects, such as second-harmonic generation (SHG), with a nonlinear susceptibility several-orders-of-magnitude higher than the 2H 2Ls. [18–24] Density functional theory (DFT) and experimental studies have revealed large conduction band and valence band splitting in the K valley, [12, 13, 25–27] leading to pronounced spin- and valley-selective carrier population [28, 29] and a built-in polarization [30] The ferroelectricity associated with this built-in polarization is attractive to several applications. For example, photovoltaic devices with high ex-
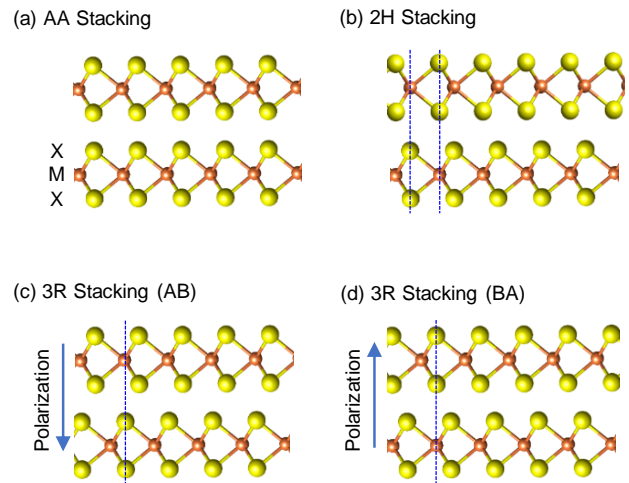

FIG. 1. Bilayer MX$_2$ with 2H and 3R stacking orders.

* huizhao@ku.edu

ternal quantum efficiency up to 16% have been demonstrated, taking advantage of the charge separation facilitated by this polarization. [31–33] Field effect transistors using 3R MX_2 as the channel material show enhanced charge mobilities compared to their 2H counterparts. [34] Furthermore, when two MX_2 monolayers are twisted by a small angle, lattice reconstruction results in arrays of nanoscale 3R domains of AB and BA with opposite polarization, which can be flipped by an electric field. Such structures could have promising applications in the so-called slide ferroelectricity. [35–40]

Despite these recent progresses, the effect of the stacking order on the excitonic dynamics in TMDs has been less studied. Excitonic dynamics play a key role in determining performance of materials in electronic and optoelectronic devices, especially 2D semiconductors where the excitons are stable at room temperature due to their large binding energies. [41, 42] Here we report a transient absorption study to compared excitonic dynamics in 1L, 2L, and bulk flakes of 2H and 3R MoS_2. We show that the exciton lifetimes in 3R 2L and bulk are about two times longer those in their 2H counterparts. The same exciton lifetime of 1L flakes exfoliated from the 3R and 2H crystals and their similar photoluminescence properties confirm that the two crystals are of comparable quality. Hence, the prolonged exciton lifetime is due to the separation of the electron and hole wavefunctions by the built-in polarization. The observed long exciton lifetime in 3R MoS_2 is consistent with their improved performance in optoelectronic devices, [31–33] and illustrate an advantage of the 3R stacking order for such applications.

II. BAND STRUCTURE AND HYPOTHESIS ON EXCITON DYNAMICS

Figure 2 shows schematically the change of the MoS_2 band structure with its thickness and stacking order, as well as its effect on the exciton dynamics. Monolayer MoS_2 (a) is a direct semiconductor with both the conduction band minimum and valence band maximum in the K valley. Hence, photoexcited electrons and holes populate the K valley, form excitons, and recombine. [3, 4] In 2L 2H MoS_2, the K valley states are largely unchanged from 1L states, while the valence band in the Γ valley rises to above the K valley. [43] In such an indirect semiconductor, excitons are formed with K-valley electrons and Γ-valley holes. These momentum-indirect excitons have a slower recombination rate since other quasiparticles or defect states have to be involved to conserve the crystalline momentum, resulting in a longer recombination lifetime than excitons in 1Ls. However, all the K-valley and Γ-valley states are layer coupled, and hence the electron and hole wavefunctions are spatially overlapped. In 2L 3R MoS_2, however, the K-valley states are decoupled and are split to two branches located in the X and M layers, respectively, while the Γ valley reminds layer coupled, as shown in (c).[12, 25–27] Consequently, the electrons populate the M layer and form excitons with the layer-coupled holes that are indirect in both momentum and real space. We expect longer exciton lifetime in 3R MoS_2 due to the reduced overlap of the electron and hole
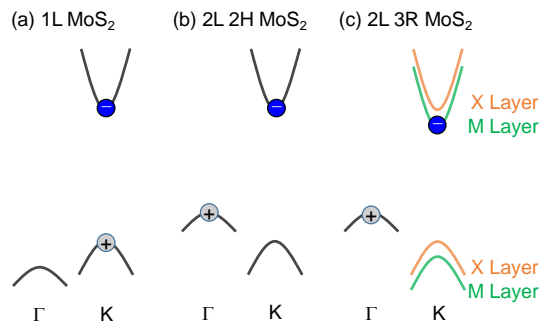

FIG. 2. Schematics of the band structure of and quasi-steady-state population of electrons (-) and holes (+) in 1L MoS_2 (a), 2L 2H MoS_2 (b), and 2L 3R MoS_2 (c)

wavefunctions.

III. SAMPLE FABRICATION AND CHARACTERIZATION

Bulk MoS_2 crystals with 3R and 2H stacking order are acquired from HQ Graphene. Bilayer (2L) and monolayer (1L) flakes are prepared by mechanical exfoliation. [44] An adhesive tape is pushed against the surface of a bulk crystal and then peeled off. Flakes residing on the tape are transferred to a polydimethylsiloxane (PDMS) substrate and are examined under an optical microscope. Thin flakes are identified according to their optical contrast. Next, the selected flakes are transferred to Si/SiO$_2$ substrates. Figure 3 shows the 2L and 1L flakes exfoliated from the two MoS_2 crystals that are used for the optical measurements.

The samples are first studied by photoluminescence (PL) spectroscopy at room temperature. A 3.06-eV continuous-wave laser beam is focused to the sample by a microscope objective lens with an incident power of 3 μW. The laser spot is about 2 μm, which is much smaller than the lateral size
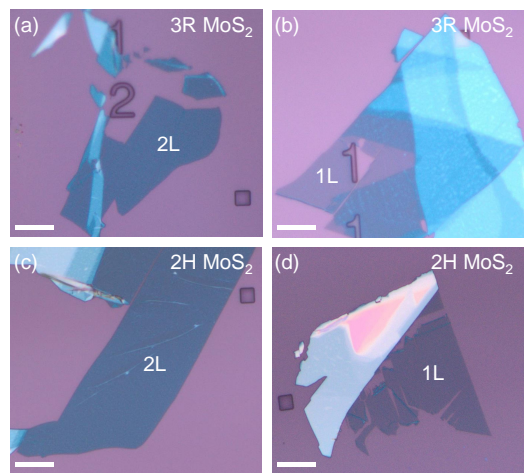

FIG. 3. Optical microscope images of samples of 2L (a) and 1L (b) exfoliated from a 3R MoS_2 crystal and those from a 2H crystal (c and d, respectively). The substrates are Si/SiO$_2$. Scale bars: 10 μm.
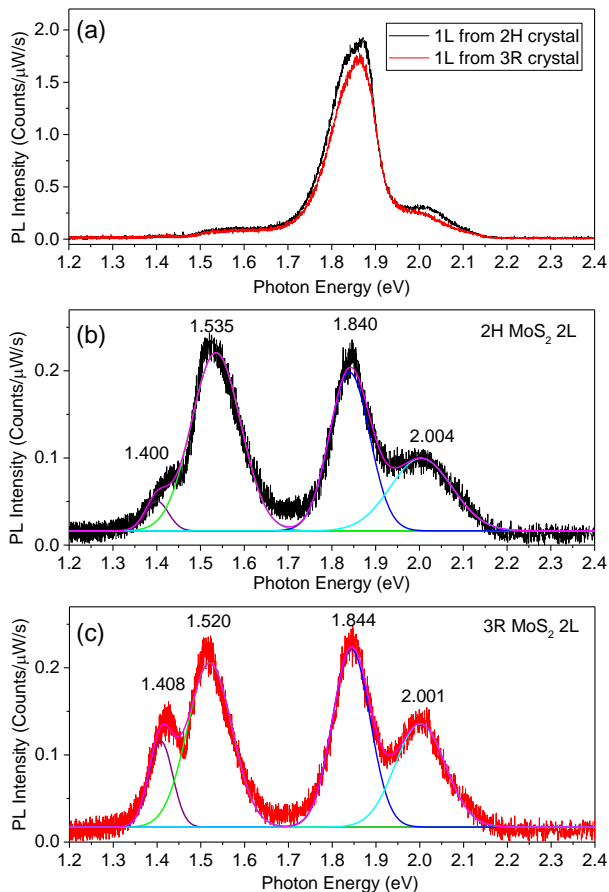
FIG. 4. Photoluminescence spectra measured from the two 1L flakes exfoliated from 2H and 3R MoS_2 crystals (a), the 2H 2L flake (b), and the 3R 2L flake (c).

of these flakes. The PL from the sample is collected by the same objective lens and measured by a spectrometer (iHR550) equipped with a thermoelectric cooled charge-coupled device camera. Figure 4(a) shows the spectra obtained from the two 1L flakes exfoliated from the 2H (black) and 3R (red) crystals, respectively. Since the two crystals only differ in interlayer stacking orders, the two 1Ls have identical structures. Indeed, their PL yields and spectra are very similar. The main peak at about 1.87 eV and the secondary peak at about 2.0 eV are consistent with the previously established K-valley A- and B-exciton energies. [3, 4] Since the ratio of A and B exciton peaks reflects the crystalline quality, [45] the similar spectra suggests that the quality of the two crystals is comparable.

Figure 4(b) shows the PL spectrum from the 2H 2L flake, measured under the same conditions as their 1Ls. The thin curves show a fit to the data with multiple Gaussian peaks, with the magenta curve being the accumulative fit. The numbers indicate the peak energies in eV. Compared to the 1L spectra, the A- and B-exciton peaks drop by about one order of magnitude, due to their reduced quasi-steady-state population. [3, 4] The pronounced peak observed at 1.535 eV is due to the indirect excitons formed by K-valley electrons and Γ-valley holes [Fig. 2(b)]. [4] In the 3R 2L MoS_2, Figure 4(c),

another peak at 1.408 eV is clearly seen. Previously, valley and layer splitting of the excitonic states in 3R MoS_2 has been revealed by reflectance spectroscopy and first-principles calculation. [46] We attribute the double-peak (1.520 and 1.408 eV) feature to the layer and valley splitting of the K-valley conduction band [Fig. 2(c)]. [17] We note that a small peak at 1.400 eV is observed in the 2H 2L flake, which is less pronounced than the 1.408-eV peak in the 3R 2L.

IV. EXCITONIC DYNAMICS IN 3R AND 2H MOS_2

The excitonic dynamics in 3R and 2H MoS_2 samples are studied by a homemade transient absorption setup in reflection geometry. A Ti-sapphire laser (Spectra-Physics Tsunami) generates 100-fs and 800-nm pulses with a repetition rate of 80 MHz and an average power of 2 W. Part of this beam is focused to a beta barium borate (BBO) crystal to generate its second harmonic at 400 nm (3.10 eV), serving as the pump pulse. The rest of the 800-nm beam pumps an optical parametric oscillator (Spectra-Physics Opal) to produce a tunable output around 1360 nm. Another BBO crystal is used to generate its second harmonic around at 680 nm (1.82 eV), serving as the probe pulse. The pump and probe pulses are co-focused to the sample by an objective lens, with a spot size of about 2 μm. At the sample, the pump and probe pulse are about 250 fs, due to the dispersive optical elements they transmit. The resulting instrumental response time is about 350 fs. The reflected probe from the sample is collimated by the objective lens and detected by a silicon photodiode. To block the co-reflected pump beam, a set of filters is placed before the photodiode. The output of the photodiode is measured by a lock-in amplifier, which is synchronized with a mechanical chopper that modulates the pump intensity at about 2 KHz. With this setup, we measure differential reflectance, which is defined as $\Delta R/R_0 = (R - R_0)/R_0$, where R and R_0 are the reflectance of the sample with and without the presence of the pump, respectively. All measurements are performed with the sample at room temperature and in ambient condition.

We first present results from the two 1L flakes exfoliated from the 2H and 3R crystals, as shown in the upper and lower rows of Fig. 5, respectively. The two flakes have the same crystalline structure, and should possess the same intrinsic properties. The goal of this measurement is to further confirm that the two crystals are of comparable quality. The 3.10-eV pump pulse injects free electron-hole pairs in the K valley, while the probe, which is tuned to the K-valley A-exciton resonance of MoS_2 (Fig. 2), monitors K-valley carrier population.

Figure 5(a) shows examples of the time-resolved differential reflectance signal of the 1L flake exfoliated from the 2H crystal measured with various pump fluences, as labeled. By using Beer's Law with a previously reported monolayer MoS_2 absorbance of 0.07 at 3.10 eV, [47, 48] we estimate that a pump fluence of 1 μJ cm^{-2}, which corresponds to a photon number density of 2×10^{12} cm^{-2}, injects a carrier density of 6×10^{10} cm^{-2}, assuming that every photon absorbed by the sample creates one electron-hole pair. The differential re-
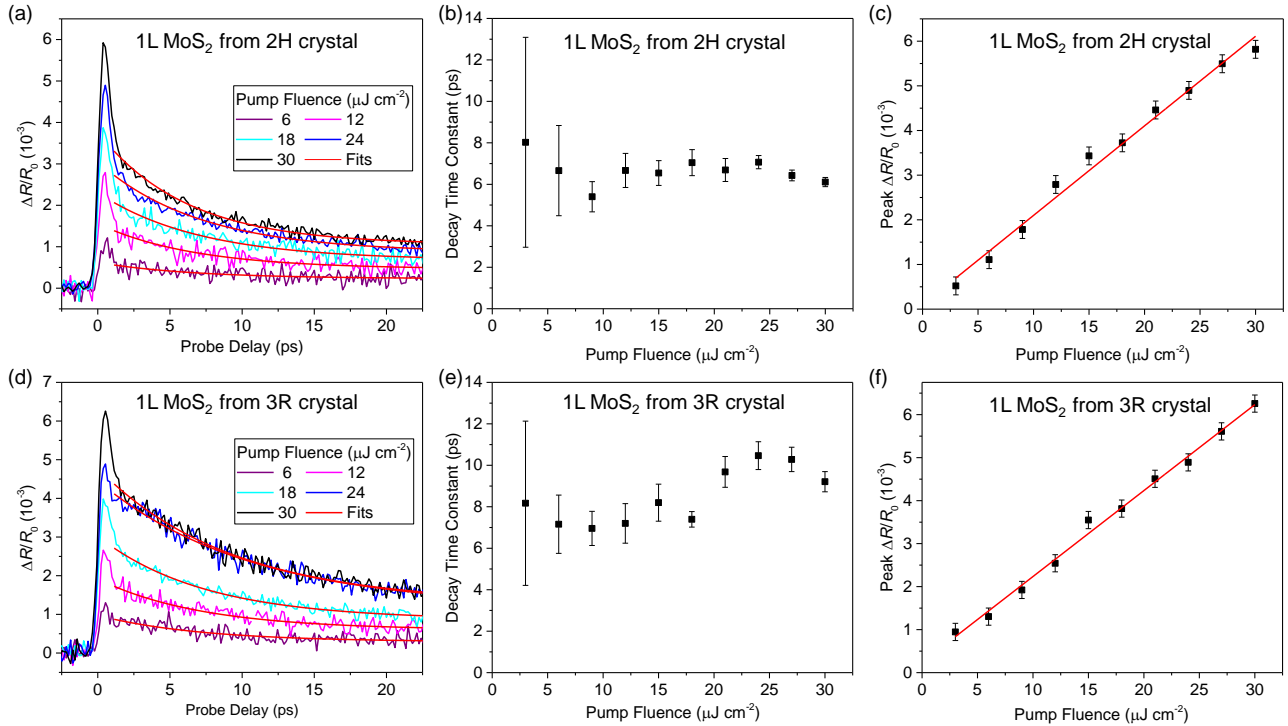
FIG. 5. (a) Differential reflectance measured from the 1L flake exfoliated from a 2H MoS$_2$ crystal with 3.10-eV pump and 1.82-eV probe pulses. The red curves are exponential fits. (b) Decay time constants deduced from the exponential fits. (c) The peak differential reflectance signal as a function of the pump fluence. The red line is a linear fit. (d), (e), and (f) are the corresponding results from the 1L flake exfoliated from a 3R MoS$_2$ crystal.

flectance signal reaches a peak rapidly, followed by a sub-ps decay. This process will be analyzed later. The decay of the signal after 1 ps is well fit by a single-exponential function, $\Delta R/R_0 = A\exp(-t/\tau) + B$, as shown by the red curves. The decay time constant is about 6 - 7 ps, as shown in Fig. 5(b), which is attributed to the recombination lifetime of excitons in 1L MoS$_2$. Figure 5(c) confirms that the peak signal is proportional to the pump fluence, which is proportional to the injected carrier density, in the fluence range studied. These features are reasonably consistent with previous experiments on exciton dynamics in 1L MoS$_2$. [49–51] The exciton lifetime shown in Fig. 5(b) is independent of the pump fluence, suggesting that the density-independent exciton dynamics dominate the process. At high densities, the strong exciton interactions in 2D semiconductors could cause exciton-exciton annihilation and reduce the exciton lifetime. [52, 53] In our experiment, the highest pump fluence used, 30 μJ cm^{-2}, injects excitons with an average distance of 7.5 nm. Exciton-exciton annihilation appears only impact the exciton dynamics insignificantly.

The lower row of Fig. 5 summarizes the results obtained from the 1L flake that is exfoliated from the 3R MoS$_2$ crystal under the same experimental conditions. The features observed are consistent with that from the 2H crystal. Hence, the 3R and 2H crystals used in this study are of comparable quality. This conclusion is consistent with the similar PL properties of the two 1L flakes shown in Fig. 4(a).

To compare the exciton dynamics in 2H and 3R 2Ls, the

same measurements are performed, with the results summarized in Fig. 6. The decay of the signal after 1 ps from the 2H 2L can no longer be fit by the single-exponential function, but is well fit by a bi-exponential function, $\Delta R/R_0 = A_1\exp(-t/\tau_1) + A_2\exp(-t/\tau_2) + B$, as shown by the red curves in Fig. 6(a). The two decay time constants, τ_1 and τ_2, are plotted as the black and red symbols, respectively, in Fig. 6(b). The fast process accounts for about 25% of the signal, with a time constant in the range of a few ps, which shows no clear fluence dependence. The slow time constant is about 40 ps, with a weak trend of increase with fluence. The signal magnitude, represented by its value at 2 ps to avoid uncertainties associated with the initial sub-ps fast decay, is proportional to the pump fluence, as shown in Fig. 6(c).

To understand the observed features, we recall that while the pump excites carriers in the K valley, the holes are expected to transfer to the Γ valley to relax their energy, as shown in Fig. 2(b). Since the probe is tuned to the K-valley optical bandgap, we can assume that the differential reflectance signal is proportional to the carrier density in the K valley. Hence, transfer of the holes from K to Γ valleys reduces the K-valley density and thus, the signal. We attribute τ_1 of a few ps to the hole intervalley scattering time. The τ_2 of about 40 ps is associated with the recombination of the Γ-K indirect excitons, which is a few times longer than the lifetime of the direct excitons in 1L MoS$_2$.

Interestingly, under the same pump conditions, the signal from the 2L flake after the τ_1 process (for example, at about
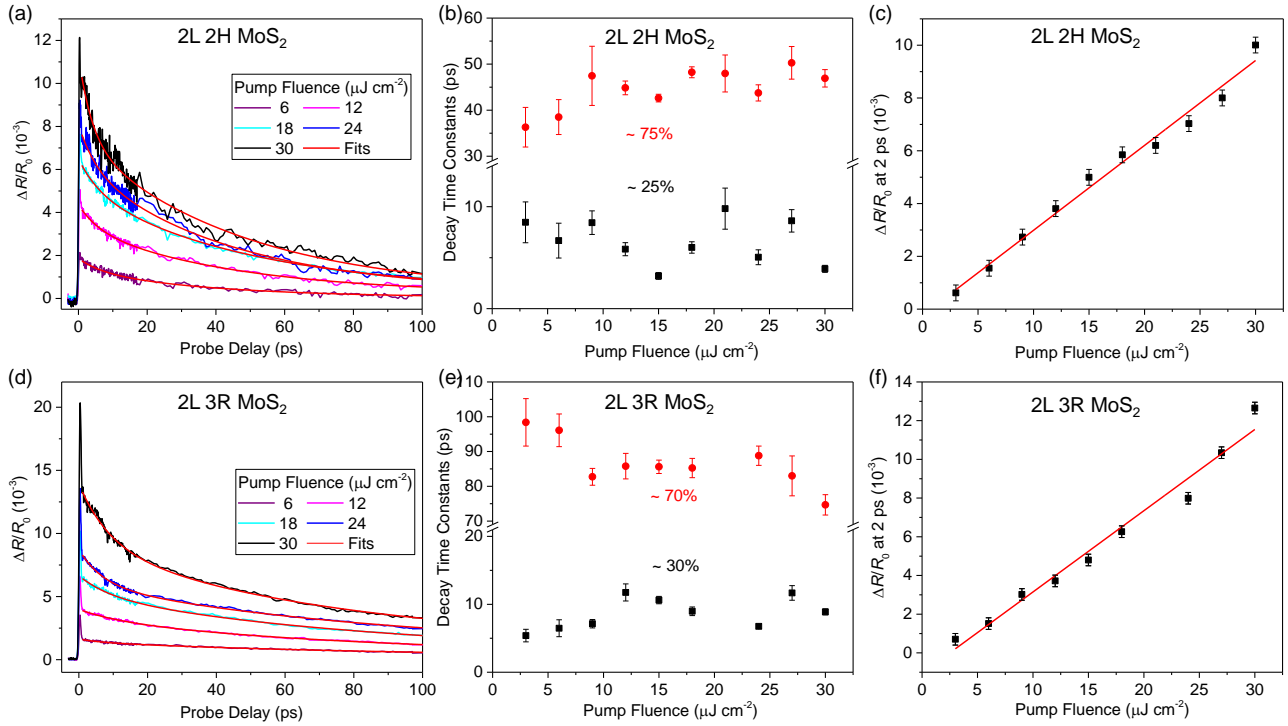
FIG. 6. (a) Differential reflectance measured from the 2L 2H MoS$_2$ flake with 3.10-eV pump and 1.82-eV probe pulses. The red curves are exponential fits. (b) Decay time constants deduced from the exponential fits. (c) The peak differential reflectance signal as a function of the pump fluence. The red line is a linear fit. (d), (e), and (f) are the corresponding results from the 2L 3R MoS$_2$ flake.

15 ps) is about two times higher than the signal from the 1L flake after its exciton formation process (for example at 2 ps). Under the same conditions, the pump-injected carrier density in 2L is two times higher than 1L because of the doubled absorbance. Meanwhile, the signal from the same density should double in 2Ls since the probe length is doubled. With both factors, the signal should be a factor of 4 larger in the 2L. However, since half of the carriers (the holes) transferred to the Γ valley, if the electrons and holes produce comparable differential reflectance, the signal from 2L after the τ_1 process should be two times larger than the signal from 1L. These are rather rough estimates. Nevertheless, the conclusion is consistent with our interpretation on the nature of the signal from 2L MoS$_2$.

We next perform the same measurements with the 2L 3R MoS$_2$ flake. As shown in the lower row of Fig. 6, the results are qualitatively similar to the 2H 2L. Most interestingly, the long time constant, τ_2, is about 85 ps. This proves our hypothesis that the built-in polarization separates the electron and hole wavefunctions in such momentum-indirect and spatially indirect excitons, and prolongs the exciton lifetime. Specifically, after the carriers are injected in the K valley by the pump, the holes transfer to the Γ valley valence band, while the electrons relax to the lower branch of the K valley conduction band, as shown in Fig. 2(c). In real space, the electrons occupy the M layer and thus the overlap of their wavefunction with that of holes, which are layer coupled, is reduced, slowing down their recombination. The τ_1 process is also in

the range of several ps, which is also attributed to the hole scattering time.

We note that the difference in the exciton lifetimes between the 2H and 3R MoS$_2$ 2Ls cannot be attributed to different crystalline qualities, such as lattice defect densities. Although mid-gap states could contribute to exciton recombination, the same exciton dynamics and PL spectra observed from the two 1L samples exfoliated from the 2H and 3R crystals prove that the densities of defect states of the two crystals are comparable.

An initial fast (sub-ps) decay of the signal is clearly visible in Fig. 6(a) and 6(d). To analysis this component, Fig. 7 summarizes the signal near zero probe delay from all the four samples discussed above. Since this component shows no fluence dependence, only the data with a pump fluence of 18 μJ cm^{-2} are plotted (black curves). The blue curve in each panel is a Gaussian function with a full width at half maximum of 0.42 ps. With the pump and probe pulses of about 0.30 ps at sample, this function represents the cross correlation of the pump and probe pulses, defining the time resolution of the setup. The integral of this function (plotted as the gray curve) well describes the rise of the signal, confirming our assessment of the time resolution. We fit the decay of the signal by a single exponential function (red curve), with the deduced decay time constant indicated in each panel. Previously, the fast decay of the transient absorption signal from TMD monolayers has been attributed to the formation of the excitons from the pump-injected free electron-hole pairs. [54–56] The deduced
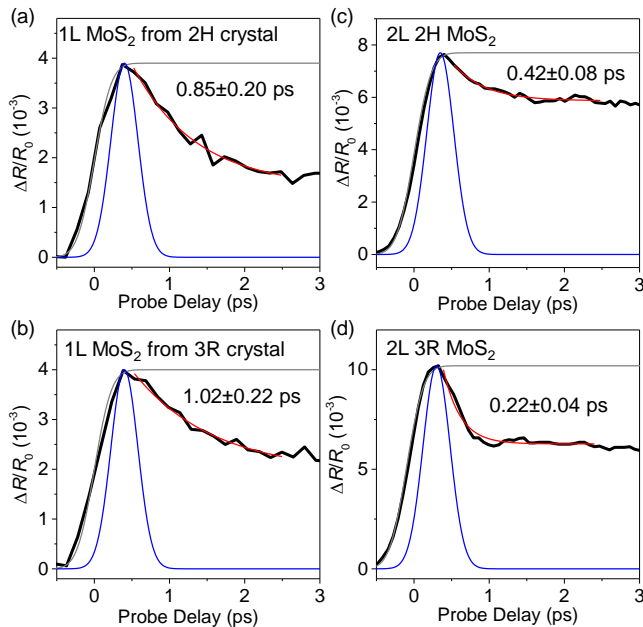
FIG. 7. Differential reflectance near zero probe delay measured with 3.10-eV and 18-μJ cm^{-2} pump and 1.820eV probe pulses from 1L (a and b) and 2L (c and d) samples. In each panel, the black curve is the data. The blue curve is a Gaussian function with a full width at half maximum of 0.42 ps, representing the time resolution. The gray curve is the integral of this Gaussian function. The red curve is an exponential fit with decay time constant labeled.

exciton formation times shown in Fig. 7(a) and 7(b) are reasonably consistent with these results. The 2L 2H MoS$_2$ shows a shorter exciton formation time compared to the 1Ls. In the 3R 2L, this time constant is as short as 0.22 ps. The more efficient exciton formation in 3R 2L could be associated with the built-in polarization. However, more experiments with better time resolution and theoretical studies are necessary to fully understand the physical mechanisms.

Finally, we compare the exciton dynamics in 2H and 3R bulk MoS$_2$ crystals by repeating the same differential reflectance measurements on a freshly exfoliated surface of each crystal. The results are summarized in Fig. 8 in the same fashion as the 1L and 2L studies. In both crystals, the signal decays bi-exponentially. We find that the exciton lifetime in the 3R MoS$_2$ crystal, represented by τ_2, is about 220 ps [Fig.

8(e)], which is about two times longer than that of 2H sample [Fig. 8(b)]. Similarly, we attribute the prolonged lifetime to the layer population of the electrons due to the built-in polarization.

V. CONCLUSION

In summary, we directly compared excitonic dynamics in 2H and 3R MoS$_2$. Monolayer, bilayer, and bulk flakes of each stacking order are exfoliated from 2H and 3R MoS$_2$ crystals. The monolayer flakes from the two crystals show similar photoluminescence properties and exciton dynamics, characterized by an exciton lifetime of a few picoseconds, suggesting that the two crystals are of similar quality. The exciton lifetimes in the 2H bilayer flake is about 40 ps, which is much longer than monolayers since excitons in 2L are momentum indirect. In 3R bilayer, the exciton lifetime is further prolonged to about 85 ps, which is attributed to the spatial separation of the electron and hole wavefunctions, since the electrons are localized in one layer due to the built-in polarization while the holes wavefunction is layer coupled. In bulk 3R MoS$_2$, the exciton lifetime is about 220 ps, which is approximately two times longer than those in 2H MoS$_2$ crystal. An additional signal decay component is identified in bilayer and bulk flakes, which is associated with an intervalley hole scattering process. The observed long exciton lifetime in 3R MoS$_2$ helps understand the improved performance of optoelectronic devices using 3R TMDs. In photovoltaic devices utilizing excitons, doubled exciton lifetime could potentially improve the power conversion efficiency by a factor of two. The detectivity of photodetectors based on excitons in such materials could also be improved similarly. Hence, our results further illustrate the advantage of the 3R stacking order of TMDs for optoelectronic applications.

[1] Q. H. Wang, K. Kalantar-Zadeh, A. Kis, J. N. Coleman, and M. S. Strano, Electronics and optoelectronics of two-dimensional transition metal dichalcogenides, Nat. Nanotechnol. 7, 699 (2012).

[2] Z. Lin, A. McCreary, N. Briggs, S. Subramanian, K. H. Zhang, Y. F. Sun, X. F. Li, N. J. Borys, H. T. Yuan, S. K. Fullerton-Shirey, A. Chernikov, H. Zhao, S. McDonnell, A. M. Lindenberg, K. Xiao, B. J. LeRoy, M. Drndic, J. C. M. Hwang, J. Park, M. Chhowalla, R. E. Schaak, A. Javey, M. C. Hersam, J. Robinson, and M. Terrones, 2D materials advances: From large scale synthesis and controlled heterostructures to improved characterization techniques, defects and applications, 2D Mater. 3, 042001 (2016).

[3] A. Splendiani, L. Sun, Y. Zhang, T. Li, J. Kim, C. Y. Chim, G. Galli, and F. Wang, Emerging photoluminescence in monolayer MoS$_2$, Nano Lett. 10, 1271 (2010).

[4] K. F. Mak, C. Lee, J. Hone, J. Shan, and T. F. Heinz, Atomically thin MoS$_2$: A new direct-gap semiconductor, Phys. Rev. Lett. 105, 136805 (2010).
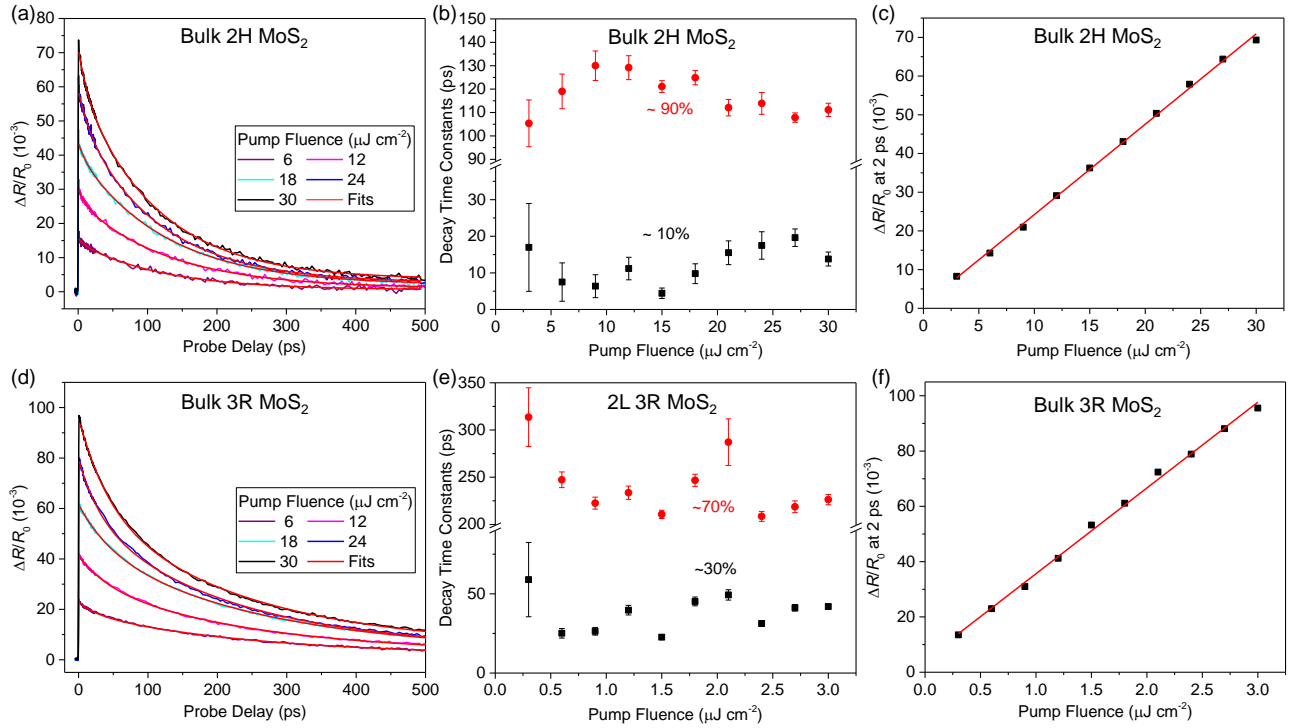
FIG. 8. (a) Differential reflectance measured from the bulk 2H MoS$_2$ crystal with 3.10-eV pump and 1.82-eV probe pulses. The red curves are exponential fits. (b) Decay time constants deduced from the exponential fits. (c) The peak differential reflectance signal as a function of the pump fluence. The red line is a linear fit. (d), (e), and (f) are the corresponding results from the bulk 3R MoS$_2$ crystal.

[5] B. Radisavljevic, A. Radenovic, J. Brivio, V. Giacometti, and A. Kis, Single-layer MoS$_2$ transistors, Nat. Nanotechnol. **6**, 147 (2011).

[6] B. Radisavljevic and A. Kis, Mobility engineering and a metal-insulator transition in monolayer MoS$_2$, Nat. Mater. **12**, 815 (2013).

[7] B. W. H. Baugher, H. O. H. Churchill, Y. Yang, and P. Jarillo-Herrero, Optoelectronic devices based on electrically tunable p-n diodes in a monolayer dichalcogenide, Nat. Nanotechnol. **9**, 262 (2014).

[8] Y. J. Zhang, T. Oka, R. Suzuki, J. T. Ye, and Y. Iwasa, Electrically switchable chiral light-emitting transistor, Science **344**, 725 (2014).

[9] J. S. Ross, P. Klement, A. M. Jones, N. J. Ghimire, J. Yan, D. G. Mandrus, T. Taniguchi, K. Watanabe, K. Kitamura, W. Yao, D. H. Cobden, and X. Xu, Electrically tunable excitonic light-emitting diodes based on monolayer WSe$_2$ p-n junctions, Nat. Nanotechnol. **9**, 268 (2014).

[10] A. Pospischil, M. M. Furchi, and T. Mueller, Solar-energy conversion and light emission in an atomic monolayer p-n diode, Nat. Nanotechnol. **9**, 257 (2014).

[11] J. Strachan, A. F. Masters, and T. Maschmeyer, 3R-MoS$_2$ in review: History, status, and outlook, ACS Appl. Energ. Mater. **4**, 7405 (2021).

[12] I. Paradisanos, S. Shree, A. George, N. Leisgang, C. Robert, K. Watanabe, T. Taniguchi, R. J. Warburton, A. Turchanin, X. Marie, I. C. Gerber, and B. Urbaszek, Controlling interlayer excitons in MoS$_2$ layers grown by chemical vapor deposition, Nat. Commun. **11**, 2391 (2020).

[13] A. Mahmoudi, M. Bouaziz, A. Chiout, G. D. Berardino, N. Ullberg, G. Kremer, P. Dudin, J. Avila, M. Silly, V. Derycke, D. Romanin, M. Pala, I. C. Gerber, J. Chaste, F. Oehler, and A. Ouerghi, Electronic properties of rhombohedrally stacked bilayer WSe$_2$ obtained by chemical vapor deposition, Phys. Rev. B **108**, 045417 (2023).

[14] J. Chen, X. Zhao, G. Grinblat, Z. Chen, S. J. R. Tan, W. Fu, Z. Ding, I. Abdelwahab, Y. Li, D. Geng, Y. Liu, K. Leng, B. Liu, W. Liu, W. Tang, S. A. Maier, S. J. Pennycook, and K. P. Loh, Homoepitaxial growth of large-scale highly organized transition metal dichalcogenide patterns, Adv. Mater. **30**, 1704674 (2018).

[15] Z. Zeng, X. Sun, D. Zhang, W. Zheng, X. Fan, M. He, T. Xu, L. Sun, X. Wang, and A. Pan, Controlled vapor growth and nonlinear optical applications of large-area 3r phase WS$_2$ and WSe$_2$ atomic layers, Adv. Funct. Mater. **29**, 1806874 (2019).

[16] D. Yang, X. Hu, M. Zhuang, Y. Ding, S. Zhou, A. Li, Y. Yu, H. Li, Z. Luo, L. Gan, and T. Zhai, Inversion symmetry broken 2D 3R-MoTe$_2$, Adv. Funct. Mater. **28**, 1800785 (2018).

[17] J. Liang, D. Yang, J. Wu, J. I. Dadap, K. Watanabe, T. Taniguchi, and Z. Ye, Optically probing the asymmetric interlayer coupling in rhombohedral-stacked MoS$_2$ bilayer, Phys. Rev. X **12**, 041005 (2022).

[18] G. A. Wagoner, P. D. Persans, E. A. Van Wagenen, and G. M. Korenowski, Second-harmonic generation in molybdenum disulfide, J. Opt. Soc. Am. B **15**, 1017 (1998).

[19] E. Mishina, N. Sherstyuk, S. Lavrov, A. Sigov, A. Mitioglu, S. Anghel, and L. Kulyuk, Observation of two polytypes of MoS$_2$ ultrathin layers studied by second harmonic generation microscopy and photoluminescence, Appl. Phys. Lett. **106**, 131901 (2015).

[20] J. Shi, P. Yu, F. Liu, P. He, R. Wang, L. Qin, J. Zhou, X. Li, J. Zhou, X. Sui, S. Zhang, Y. Zhang, Q. Zhang, T. C. Sum,

X. Qiu, Z. Liu, and X. Liu, 3R MoS$_2$ with broken inversion symmetry: A promising ultrathin nonlinear optical device, Adv. Mater. **29**, 1701486 (2017).

[21] C. He, L. Zhu, Y. Huang, W. Du, M. Qi, Y. Zhou, Q. Zhao, and X. Xu, Accurately controlling angle-resolved second harmonic generation by stacking orders from a MoS$_2$ homobilayer, J. Phys. Chem. C **126**, 10584 (2022).

[22] M. Zhao, Z. L. Ye, R. Suzuki, Y. Ye, H. Y. Zhu, J. Xiao, Y. Wang, Y. Iwasa, and X. Zhang, Atomically phase-matched second-harmonic generation in a 2D crystal, Light-Sci. Appl. **5**, e16131 (2016).

[23] C. T. Le, J. Kim, F. Ullah, A. D. Nguyen, T. N. N. Tran, T. E. Le, K. H. Chung, H. Cheong, J. I. Jang, and Y. S. Kim, Effects of interlayer coupling and band offset on second harmonic generation in vertical MoS$_2$/MoS$_{2(1−x)}$Se$_{2x}$ structures, ACS Nano **14**, 4366 (2020).

[24] D. Zhang, Z. Zeng, Q. Tong, Y. Jiang, S. Chen, B. Zheng, J. Qu, F. Li, W. Zheng, F. Jiang, H. Zhao, L. Huang, K. Braun, A. J. Meixner, X. Wang, and A. Pan, Near-unity polarization of valley-dependent second-harmonic generation in stacked TMDC layers and heterostructures at room temperature, Adv. Mater. **32**, 1908061 (2020).

[25] J. G. He, K. Hummer, and C. Franchini, Stacking effects on the electronic and optical properties of bilayer transition metal dichalcogenides MoS$_2$, MoSe$_2$, WS$_2$, and WSe$_2$, Phys. Rev. B **89**, 075409 (2014).

[26] A. Kormanyos, V. Zolyomi, V. I. Fal'ko, and G. Burkard, Tunable berry curvature and valley and spin hall effect in bilayer MoS$_2$, Phys. Rev. B **98**, 035408 (2018).

[27] A. Yan, W. Chen, C. Ophus, J. Ciston, Y. Lin, K. Persson, and A. Zettl, Identifying different stacking sequences in few-layer CVD-grown MoS$_2$ by low-energy atomic-resolution scanning transmission electron microscopy, Phys. Rev. B **93**, 041420(R) (2016).

[28] R. Suzuki, M. Sakano, Y. J. Zhang, R. Akashi, D. Morikawa, A. Harasawa, K. Yaji, K. Kuroda, K. Miyamoto, T. Okuda, K. Ishizaka, R. Arita, and Y. Iwasa, Valley-dependent spin polarization in bulk MoS$_2$ with broken inversion symmetry, Nat. Nanotechnol. **9**, 611 (2014).

[29] X. Zhang, J. Zhou, S. Q. Li, Y. Wang, S. Zhang, Y. Liu, J. Gao, J. Zhao, W. Wang, R. Yu, W. Zhang, N. Liu, J. Nie, L. He, and R. Dou, Enhanced valley polarization of bilayer MoSe$_2$ with variable stacking order and interlayer coupling, J. Phys. Chem. Lett. **12**, 5879 (2021).

[30] J. Park, I. W. Yeu, G. Han, C. Jang, J. Y. Kwak, C. S. Hwang, and J. H. Choi, Optical control of the layer degree of freedom through Wannier-stark states in polar 3R MoS$_2$, J. Phys.-Condes. Matter **31**, 315502 (2019).

[31] D. Yang, J. Wu, B. T. Zhou, J. Liang, T. Ideue, T. Siu, K. M. Awan, K. Watanabe, T. Taniguchi, Y. Iwasa, M. Franz, and Z. Ye, Spontaneous-polarization-induced photovoltaic effect in rhombohedrally stacked MoS$_2$, Nat. Photonics **16**, 469 (2022).

[32] J. Wu, D. Yang, J. Liang, M. Werner, E. Ostroumov, Y. Xiao, K. Watanabe, T. Taniguchi, J. I. Dadap, D. Jones, and Z. Ye, Ultrafast response of spontaneous photovoltaic effect in 3R-MoS$_2$-based heterostructures, Sci. Adv. **8**, eade3759 (2022).

[33] Y. Dong, M. M. Yang, M. Yoshii, S. Matsuoka, S. Kitamura, T. Hasegawa, N. Ogawa, T. Morimoto, T. Ideue, and Y. Iwasa, Giant bulk piezophotovoltaic effect in 3R-MoS$_2$, Nat. Nanotechnol. **18**, 36 (2023).

[34] X. Li, X. Shi, D. Marian, D. Soriano, T. Cusati, G. Iannaccone, G. Fiori, Q. Guo, W. Zhao, and Y. Wu, Rhombohedral-stacked bilayer transition metal dichalcogenides for high-performance atomically thin CMOS devices, Sci. Adv. **9**, eade5706 (2023).

[35] J. Sung, Y. Zhou, G. Scuri, V. Zolyomi, T. I. Andersen, H. Yoo, D. S. Wild, A. Y. Joe, R. J. Gelly, H. Heo, S. J. Magorrian, D. Berube, A. M. M. Valdivia, T. Taniguchi, K. Watanabe, M. D. Lukin, P. Kim, V. I. Fal'ko, and H. Park, Broken mirror symmetry in excitonic response of reconstructed domains in twisted MoSe$_2$/MoSe$_2$ bilayers, Nat. Nanotechnol. **15**, 750 (2020).

[36] A. Weston, Y. C. Zou, V. Enaldiev, A. Summerfield, N. Clark, V. Zolyomi, A. Graham, C. Yelgel, S. Magorrian, M. W. Zhou, J. Zultak, D. Hopkinson, A. Barinov, T. H. Bointon, A. Kretinin, N. R. Wilsons, P. H. Beton, V. I. Fal'ko, S. J. Haigh, and R. Gorbachev, Atomic reconstruction in twisted bilayers of transition metal dichalcogenides, Nat. Nanotechnol. **15**, 592 (2020).

[37] T. I. Andersen, G. Scuri, A. Sushko, K. D. Greve, J. Sung, Y. Zhou, D. S. Wild, R. J. Gelly, H. Heo, D. Berube, A. Y. Joe, L. A. Jauregui, K. Watanabe, T. Taniguchi, P. Kim, H. Park, and M. D. Lukin, Excitons in a reconstructed moire potential in twisted WSe$_2$/WSe$_2$ homobilayers, Nat. Mater. **20**, 480 (2021).

[38] N. Tilak, G. Li, T. Taniguchi, K. Watanabe, and E. Y. Andrei, Moire potential, lattice relaxation, and layer polarization in marginally twisted MoS$_2$ bilayers, Nano Lett. **23**, 73 (2023).

[39] P. Meng, Y. Z. Wu, R. J. Bian, E. Pan, B. Dong, X. X. Zhao, J. G. Chen, L. S. Wu, Y. Q. Sun, Q. D. Fu, Q. Liu, D. Shi, Q. Zhang, Y. W. Zhang, Z. Liu, and F. C. Liu, Sliding induced multiple polarization states in two-dimensional ferroelectrics, Nat. Commun. **13**, 7696 (2022).

[40] X. R. Wang, K. Yasuda, Y. Zhang, S. Liu, K. Watanabe, T. Taniguchi, J. Hone, L. Fu, and P. Jarillo-Herrero, Interfacial ferroelectricity in rhombohedral-stacked bilayer transition metal dichalcogenides, Nat. Nanotechnol. **17**, 367 (2022).

[41] A. Chernikov, T. C. Berkelbach, H. M. Hill, A. Rigosi, Y. Li, O. Aslan, D. R. Reichman, M. S. Hybertsen, and T. F. Heinz, Exciton binding energy and nonhydrogenic Rydberg series in monolayer WS$_2$, Phys. Rev. Lett. **113**, 076802 (2014).

[42] K. He, N. Kumar, L. Zhao, Z. Wang, K. F. Mak, H. Zhao, and J. Shan, Tightly bound excitons in monolayer WSe$_2$, Phys. Rev. Lett. **113**, 026803 (2014).

[43] H. G. Kim and H. J. Choi, Thickness dependence of work function, ionization energy, and electron affinity of Mo and W dichalcogenides from DFT and GW calculations, Phy. Rev. B **103**, 085404 (2021).

[44] F. Ceballos, P. Zereshki, and H. Zhao, Separating electrons and holes by monolayer increments in van der Waals heterostructures, Phys. Rev. Mater. **1**, 044001 (2017).

[45] K. M. McCreary, A. T. Hanbicki, S. V. Sivaram, and B. T. Jonker, A- and B-exciton photoluminescence intensity ratio as a measure of sample quality for trancition metal dichalcogenide monolayers, APL Mater. **6**, 111106 (2018).

[46] R. Akashi, M. Ochi, S. Bordacs, R. Suzuki, Y. Tokura, Y. Iwasa, and R. Arita, Two-dimensional valley electrons and excitons in noncentrosymmetric 3R-MoS$_2$, Phys. Rev. Appl. **4**, 014002 (2015).

[47] T. Zheng, Y.-C. Lin, Y. L. Yu, P. Valencia-Acuna, A. A. Puretzky, R. Torsi, C. Z. Liu, I. N. Ivanov, G. Duscher, D. B. Geohegan, Z. H. Ni, K. Xiao, and H. Zhao, Excitonic dynamics in Janus MoSSe and WSSe monolayers, Nano Lett. **21**, 931 (2021).

[48] Y. Li, A. Chernikov, X. Zhang, A. Rigosi, H. M. Hill, A. M. van der Zande, D. A. Chenet, E.-M. Shih, J. Hone, and T. F. Heinz, Measurement of the optical dielectric function of monolayer transition-metal dichalcogenides: MoS$_2$, MoSe$_2$, WS$_2$, and WSe$_2$, Phys. Rev. B **90**, 205422 (2014).

[49] W. Wang, N. Sui, X. Chi, Z. Kang, Q. Zhou, L. Li, H. Zhang, J. Gao, and Y. Wang, Investigation of hot carrier cooling dy-

namics in monolayer MoS_2, J. Phys. Chem. Lett. **12**, 861 (2021).

[50] W. Lee, Y. Lin, L. S. Lu, W. C. Chueh, M. Liu, X. Li, W. H. Chang, R. A. Kaindl, and C. K. Shih, Time-resolved arpes determination of a quasi-particle band gap and hot electron dynamics in monolayer MoS_2, Nano Lett. **21**, 7363 (2021).

[51] P. Valencia-Acuna, S. Amos, H. Peelaers, and H. Zhao, Energy-valley-dependent charge transfer in few-layer transition metal dichalcogenide heterostructures, Phys. Rev. B **108**, 085302 (2023).

[52] N. Kumar, Q. Cui, F. Ceballos, D. He, Y. Wang, and H. Zhao, Exciton-exciton annihilation in $MoSe_2$ monolayers, Phys. Rev. B **89**, 125427 (2014).

[53] D. Sun, Y. Rao, G. A. Reider, G. Chen, Y. You, L. Brezin, A. R. Harutyunyan, and T. F. Heinz, Observation of rapid exciton-exciton annihilation in monolayer molybdenum disulfide, Nano Lett. **14**, 5625 (2014).

[54] F. Ceballos, Q. Cui, M. Z. Bellus, and H. Zhao, Exciton formation in monolayer transition metal dichalcogenides, Nanoscale **8**, 11681 (2016).

[55] P. Steinleitner, P. Merkl, P. Nagler, J. Mornhinweg, C. Schuller, T. Korn, A. Chernikov, and R. Huber, Direct observation of ultrafast exciton formation in a monolayer of WSe_2, Nano Lett. **17**, 1455 (2017).

[56] P. Zereshki, P. Valencia-Acuna, and H. Zhao, All-optical control of charge transfer and interlayer excitons in transition metal dichalcogenide heterostructures, Phys. Rev. B **103**, 165416 (2021).